Petroleum Science 20 (2023) 2399–2412

Contents lists available at ScienceDirect

Petroleum Science

journal homepage: www.keaipublishing.com/en/journals/petroleum-science

Original Paper

Performance of large-diameter pneumatic down-the-hole (DTH) hammers: A focus on influences of the hammer structure

Pin-Lu Cao, Hong-Yu Cao, Jin-E Cao, Cheng-Da Wen, Bao-Yi Chen, Shan-Shan Yao*

College of Construction Engineering, Jilin University, No.938 Ximinzhu Str, Changchun, Jilin, 130061, China

ARTICLE INFO

Article history:
Received 1 August 2022
Received in revised form
8 December 2022
Accepted 23 February 2023
Available online 27 February 2023

Edited by Jia-Jia Fei

Keywords:
Pneumatic down-the-hole (DTH) hammer
Computational fluid dynamics
Dynamic mesh
Gas turbulent flow
Piston impact performance

ABSTRACT

Pneumatic down-the-hole (DTH) hammer has been extensively used in air drillings through hard and ultra-hard geological formations. Numerical modeling can offer close observation on the working behaviors by visualizing internal pressure status as well as provide reliable performance predictions for large-diameter DTH hammers to which conventional empirical and experimental approaches cannot be applied. In this study, CFD simulations coupled with dynamic meshing are utilized to simulate the air flow and piston movement inside the large-diameter DTH hammers. The numerical modeling scheme is verified against a theoretical model published in literature. Effects of structural parameters on hammer performance, including piston mass, piston upper-end diameter, piston groove diameter, and lengths of intake and exhaust stroke in both front and rear chambers, are analyzed in detail by virtue of sets of numerical simulations. The simulations suggest that changing the intake stroke of front chamber has a negligible influence on hammer performance while increasing the piston groove would lower all the four indicators of hammer performance, including impact energy, impact frequency, maximum stroke, and air consumption rate. Changing the other structural parameters demonstrates mixed effects on the performance indicators. Based on the numerical simulations, a large GQ-400 DTH hammer has been designed for reduced air consumption rate and tested in a field drilling practice. The air drilling test with the designed hammer provided a penetration rate 1.7 times faster than that of conventional mud drilling.
© 2023 The Authors. Publishing services by Elsevier B.V. on behalf of KeAi Communications Co. Ltd. This is an open access article under the CC BY-NC-ND license (http://creativecommons.org/licenses/by-nc-nd/4.0/).

1. Introduction

Air drilling with a pneumatic down-the-hole (DTH) hammer, i.e., air hammer, is known as one of the advanced rotary percussive drilling technologies applicable to moderately-to-extremely hard rock formations (Chiang and Stamm, 1998). This kind of drilling technology has been extensively utilized in oil and gas exploitation (Lian et al., 2015; Zhang et al., 2016), mineral exploration, geothermal resource utilization, civil engineering construction, etc. (Juvani et al., 2016; Cao et al., 2016; Timonin et al., 2018; Yao et al., 2018). Fig. 1 demonstrates the structure of a typical pneumatic DTH hammer. The hammer consists of a connector, a central tube, an outer cylinder, an inner tube, a piston, a spacer bush, and a splined sleeve. When high-pressure air rushes into the pneumatic hammer through the connector, a part of the air's energy is transferred to the hammer piston. Then, the energized piston moves down to hit the drill bit at a frequency, transfers most of its kinetic energy to the drill bit, and carries the drill bit to percuss rocks. An impact force brought about by the percussion, coupled with the force resulting from drill rig rotation, breaks rocks. Finally, the broken rocks (or rock cuttings) are transported up towards the land surface by the compressed air through normal or reverse circulation in annulus (Yin et al., 2013). The application of a pneumatic DTH hammer in the drillings through brittle and hard rock formations can increase the penetration rate by several times when compared against the utilization of a tri-cone bit or a polycrystalline diamond compact bit. Furthermore, utilizing an air hammer allows a drilling process to proceed with a minimal drill load and a minor torque on drill bit. This impressive feature of air hammers promotes straight-line drilling.

Generally, the performance of a pneumatic hammer can be characterized by several indicators, including energy W and frequency F of piston impact, maximum stroke L_{max} that the piston ever reaches, air consumption rate Q, and impact efficiency which is the ratio of the hammer's output (or impact) power over input

* Corresponding author.
E-mail address: shanshanyao@jlu.edu.cn (S.-S. Yao).

https://doi.org/10.1016/j.petsci.2023.02.028
1995-8226/© 2023 The Authors. Publishing services by Elsevier B.V. on behalf of KeAi Communications Co. Ltd. This is an open access article under the CC BY-NC-ND license (http://creativecommons.org/licenses/by-nc-nd/4.0/).

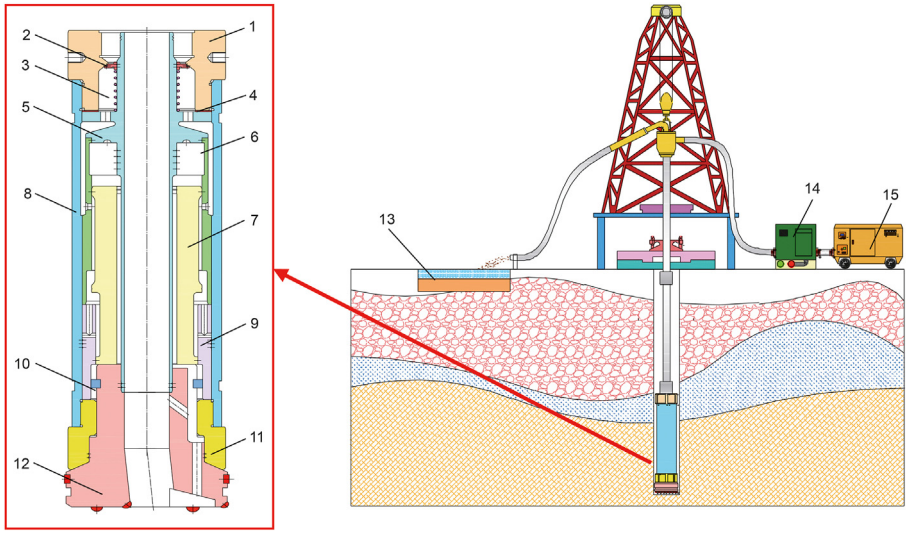

1– Connector; 2– Valve; 3– Disc spring; 4– Adjusting washer; 5– Central tube; 6– Inner tube; 7– Piston; 8– Outer cylinder; 9– Spacer bush; 10– Semi-circle clip; 11– Spline sleeve; 12– Drill bit; 13– Grit reservoir; 14– Booster; 15- Air compressor.

Fig. 1. 2D demonstration of air drilling with a pneumatic DTH hammer.

power. Investigations on the performance of pneumatic hammers have long relied on experiments and empirical correlations (Chiang and Stamm, 1998; Kim et al., 2019; Yin, 2020). However, experimental studies are always time-consuming and costly, especially for the hammers of large diameters. Empirical studies generally make assumptions for simplification purposes, and therefore, few details of a hammer's working behaviors can be obtained. Numerical modeling of a pneumatic DTH hammer drilling system can contribute to the hammer's design and performance evaluation without above concerns. Chiang and Stamm (1998) developed a generic non-linear model to simulate the impact performance of air hammers based on the impulse momentum principle. But one of the factors that the non-linear modeling method took required field tests under various conditions of rock tenacity and drill-bit shape. Chiang and Elıas (2000) developed 1D finite element models of a pneumatic DTH hammer drilling system. Later Chiang and Elıas (2008) upgraded the numerical models from 1D to 3D. Their results indicated that the geometry and mass distribution of a piston can affect the energy transfer between a drill bit and rocks. Chiang and Elıas (2000, 2008) further found out that if the piston moves away from the drill bit before rocks can reflect any stress wave back onto it, most of the energy carried by the drill bit can be finally absorbed by the rocks. In addition, when rock hardness increased, the maximum magnitude of the impact force induced by the drill bit percussion increased but the penetration depth travelled by the drill bit decreased. Song et al. (2019) built 3D finite element models using ABAQUS. Their numerical results supported that a higher energy carried by the piston in an air hammer would weaken the elastic energy rebound towards the drill bit from rocks and therefore, enhance the energy transfer efficiency between the drill bit and rocks. Later Song et al. (2021) improved their numerical models by considering both the axial and torsional percussions of a drill bit. Their results suggested that the axial percussion can significantly impact the energy transfer efficiency of the torsional percussion, while the energy transfer occurring in the axial percussion can be marginally influenced by the torsional percussion. Yin (2020) modeled the impact performance of air hammers by developing sets of differential equations and solving the equations after taking several empirical coefficients. Yin's method (Yin, 2020) is mainly based on the model generated by Chiang and Stamm (1998). The model of Chiang and Stamm (1998) predicted an impact frequency resembling the frequency measured in field test with a discrepancy in the order of 10%. Yin's modeling (Yin, 2020) offered acceleration, velocity, and displacement of a piston in an air hammer. In 2019, Zhang et al. (2019) built simulations of piston movement in a conventional air hammer of nominal outside diameter 142 mm. Nevertheless, only one structural parameter, i.e., piston mass, was tested in their analysis of DTH hammers' performance. After reviewing above and many other numerical models in literature (Lundberg, 1982; Bu et al., 2009; Franca, 2011; Luo et al., 2016; Cao et al., 2018; He et al., 2018), we conclude that most of the numerical models focused on the performance of the drill bit while the performance of an air hammer actuating the drill bit has not been detailed under various structural parameters.

This study aims to investigate in detail how the structure of the DTH hammers that are larger than conventional ones can influence their performance by virtue of numerical modeling. Dynamics of the air flow in DTH hammers as well as dynamics of the resultant piston movement are simulated with eight structural parameters covered in order to examine the role of an air hammer's structure in air drilling thoroughly. Variations of impact energy, impact frequency, maximum stroke, and air consumption rate against the structural parameters are analyzed. A large-diameter DTH hammer is designed accordingly with an aim of reducing air consumption rate and further applied in a field drilling practice for performance check.

2. Return and impact stroke

Inside an air hammer a piston can be found to be between a front chamber and a rear chamber. Performance of a pneumatic DTH hammer depends on the air flows in chambers as well as the resultant piston movement. Fig. 2 displays one round of piston up-and-down movement and the associated gas flows in the front and rear chambers. Fig. 2a–f mark six key positions of a piston during its upward movement, i.e., return stroke, while Fig. 2g–l emphasize the same six key positions again but during subsequent downward movement, i.e., impact stroke. During the piston movement from the initial position in Fig. 2a–b, the inlet port keeps open to the front chamber, while the rear chamber stays connected to the

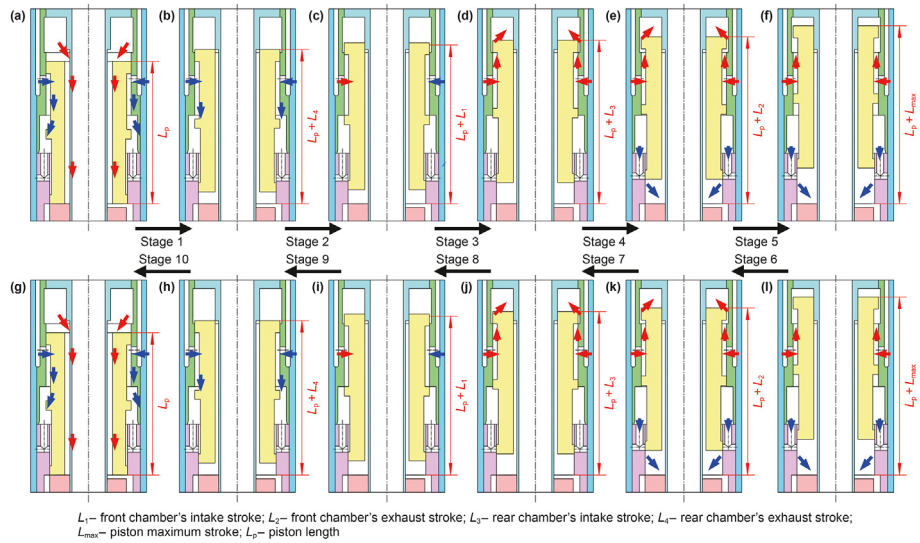

Fig. 2. (**a**)–(**e**) Piston up-movement in the return stroke and (**f**)–(**j**) piston down-movement in the impact stroke. Air flows in the rear chamber are marked by red arrows while air flows in the front chamber are marked by blue arrows.

outlet channel. Air rushes into the front chamber, whereas the rear chamber discharges air. As the piston moves up from Fig. 2b towards Fig. 2c, the rear chamber shrinks and gets disconnected from the outlet channel. The air confined in this rear chamber is therefore compressed. As the piston climbs towards Fig. 2d from Fig. 2c, the front chamber continues expanding and gets disconnected from the inlet port. The air left inside this front chamber expands accordingly. With the piston rising from Fig. 2d–e, the inlet port turns connected to the rear chamber. This open rear chamber lets running air in for the first time in this round of piston movement. Then the piston continues rising towards Top Dead Center (TDC) shown in Fig. 2f. In Fig. 2f, the outlet channel becomes open to the front chamber for the first time in this round of piston movement. Accordingly, the air expansion in the front chamber stops and air discharge starts. The piston down-movement shown in Fig. 2g–l is a totally reversed process when compared against Fig. 2a–f. When the piston returns to the initial position after one round of up-and-down movement, most of its impact energy has been transferred to a drill bit. Table 1 summarizes the total ten stages of piston movement and the corresponding air flow statuses in chambers.

3. Numerical modeling

Diameters of conventional DTH hammers usually do not exceed 200 mm. The hammers larger than conventional ones are very heavy as well as consume a large amount of air. Therefore, numerical modeling of large-diameter hammers is more efficient than experimental investigation. This study aims to explore the influence of GQ-400 DTH hammer structure on its performance by virtue of numerical simulations. Fig. 3 marks all the diameters and lengths that can characterize a GQ-400 DTH hammer's outside and inside structure, and Table 2 summarizes values of the structural parameters taken into numerical simulations.

3.1. Modeling the air flow inside chambers

ANSYS Fluent CFD package is utilized to model the air flows inside hammer chambers. In this study, the compressible transient air flow inside the front and rear chambers is described with Navier-Stokes (N-S) equations as below:

Table 1
Features of piston movement and air flows in pneumatic DTH hammer.

	Stage No.	Piston displacement	Piston movement direction	Front chamber status	Air flow in front chamber	Rear chamber status	Air flow in rear chamber
Return stroke	1	$0 \le L < L_4$	Up	Open inlet/closed outlet	Air intake	Closed inlet/open outlet	Air discharge
	2	$L_4 \le L < L_1$	Up	Open inlet/closed outlet	Air intake	Closed inlet/closed outlet	Air compression
	3	$L_1 \le L < L_3$	Up	Closed inlet/closed outlet	Air expansion	Closed inlet/closed outlet	Air compression
	4	$L_3 \le L < L_2$	Up	Closed inlet/closed outlet	Air expansion	Open inlet/closed outlet	Air intake
	5	$L_2 \le L < L_{max}$	Up	Closed inlet/open outlet	Air discharge	Open inlet/closed outlet	Air intake
Impact stroke	6	$L_2 \le L < L_{max}$	Down	Closed inlet/open outlet	Air discharge	Open inlet/closed outlet	Air intake
	7	$L_3 \le L < L_2$	Down	Closed inlet/closed outlet	Air compression	Open inlet/closed outlet	Air intake
	8	$L_1 \le L < L_3$	Down	Closed inlet/closed outlet	Air compression	Open inlet/closed outlet	Air expansion
	9	$L_4 \le L < L_1$	Down	Open inlet/closed outlet	Air intake	Open inlet/closed outlet	Air expansion
	10	$0 \le L < L_4$	Down	Open inlet/closed outlet	Air intake	Closed inlet/closed outlet	Air discharge

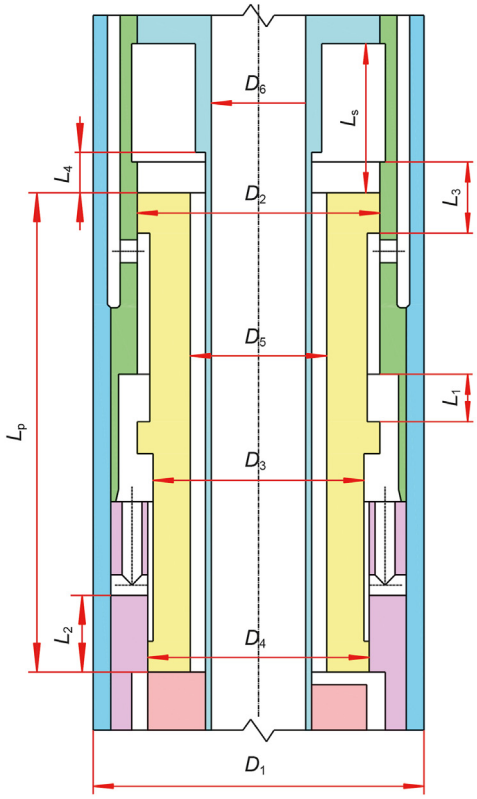

D_1– External diameter; D_2– Piston upper-end diameter;
D_3– Piston groove diameter; D_4– Piston bottom diameter;
D_5– Piston inner diameter; D_6– Inner diameter of central tube;
L_p– Piston length; L_s– Rear chamber's length;
L_1– Front chamber's intake stroke; L_2– Front chamber's exhaust stroke;
L_3– Rear chamber's intake stroke; L_4– Rear chamber's exhaust stroke.

Fig. 3. The GQ-400 DTH hammer's structure with its characteristic sizes marked.

Table 2
Structural parameters of a GQ-400 DTH hammer.

External diameter of the hammer D_1, mm	400
Piston upper-end diameter D_2, mm	295
Piston groove diameter D_3, mm	260
Piston bottom diameter D_4, mm	270
Piston inner diameter D_5, mm	141
Inner diameter of the central tube D_6, mm	95
Piston length L_p, mm	720
Rear chamber's length L_s, mm	175
Front chamber's intake stroke L_1, mm	59
Front chamber's exhaust stroke L_2, mm	108
Rear chamber's intake stroke L_3, mm	82
Rear chamber's exhaust stroke L_4, mm	44

$$\frac{\partial \rho_a}{\partial t} + \nabla \cdot (\rho_a \mathbf{u}) = 0 \square \tag{1}$$

$$\rho_a \left(\frac{\partial \mathbf{u}}{\partial t} + \mathbf{u} \cdot \nabla \mathbf{u} \right) = -\nabla P + \nabla \cdot \tau + \rho_a g, \tag{2}$$

$$\frac{\partial}{\partial t}\left[\rho_a\left(e + \frac{1}{2}\mathbf{u}^2\right)\right] + \nabla \cdot \left[\rho_a \mathbf{u}\left(e + \frac{1}{2}\mathbf{u}^2\right)\right] = \nabla \cdot (K \nabla T) + \nabla \cdot (-P\mathbf{u} + \tau \cdot \mathbf{u}) = \mathbf{u} \cdot \rho_a g \tag{3}$$

where ρ_a is air density, t is time variable, $\mathbf{u}$ is gas velocity vector, P is gas pressure, τ is stress tensor and equals to $\mu(\nabla \mathbf{u} + (\nabla \mathbf{u})^T) + \nabla \cdot \left[-\frac{2}{3}(\nabla \cdot \mathbf{u})\mathbf{I}\right]$ for compressible Newtonian fluids, μ is gas viscosity, $\mathbf{g}$ is gravitational acceleration, T is air temperature, K is thermal conductivity, and e is gas internal energy per unit mass. According to Fluent User's Guide, ideal gas equation of state is determined to be a proper fluid model in characterizing the properties of air:

$$P = \rho_a R_g T, \tag{4}$$

where R_g is specific gas constant. Eq. (4) suggests that air density is changing when the operating pressure and temperature change. Pressure Inlet Boundary condition and Pressure Outlet Boundary condition from ANSYS Fluent CFD simulator are applied on the inlet and outlet of hammer chamber, respectively. No-slip boundary condition is applied to all the walls of the hammer including the piston's surfaces. Different from this transient flow process, heat transfer inside a DTH hammer is considered as a quasi-static adiabatic process. Heat transfer generated by friction resistance and DTH hammer rotation is ignored and gas temperature at chamber inlet is fixed to be 300 K. Besides, energy equation is utilized to calculate the heat generated by high pressure compression.

Reynolds numbers of the gas flows inside a DTH hammer can be remarkably high, causing the gas flows to be in turbulent flow regime (Kim et al., 2019; Zhang et al., 2019). This study uses a Reynolds Averaged Navier-Stokes (RANS) formulation of N-S equations to average gas velocity and pressure fields in time domain. RANS formulation can provide effective, robust, and reasonably accurate solutions for turbulent flow simulations. RANS formulation brings about two additional variables, i.e., turbulent kinetic energy k and turbulent dissipation ε, and correspondingly, two additional equations named as k-ε equations (Versteeg and Malalasekera, 2007). This study chooses the Re-Normalisation Group (RNG) method (Yakhot et al., 1992) to develop the k-ε equations. Details of RNG k-ε equations can be found in Ansys Fluent Theory Guide (ANSYS Inc, 2019). All the governing equations are finally solved with the pressure-based solver Coupled in ANSYS Fluent. When solving the equations, second-order upwind is further utilized in the spatial discretization of computational domains. In addition, scalable wall functions have been applied to avoid the possible divergence in a solution process when the gas flow velocity gradients around walls become too high in the turbulent flow regime.

3.2. Modeling the piston movement

Piston in a pneumatic DTH hammer is driven by an external axial force and the gravitational force together to move linearly forward and backward along the hammer's axis. The axial force is generated by the air pressure difference between front and rear chambers. And the axial force is always considered not to deform the piston. Accordingly, the piston acceleration a can be calculated as

$$a = \frac{1}{m}\left(P_f A_{fp} - P_b A_{bp} - P_c A_{ps}\right) - g, \tag{5}$$

where m is the piston mass, P_f is gas pressure in the front chamber, A_{fp} is the area of the piston exposed to the front chamber, P_b is gas pressure in the rear chamber, A_{bp} is the area of the piston exposed to the rear chamber, P_c is backpressure at bottomhole, A_{ps} is effective base area of the piston exposed to the bottomhole. Piston acceleration could be considered during a small-enough time step

in the discretization of time domain. Accordingly, piston velocity and distance travelled by the piston during i-th time step (t_{i-1}, t_i) are:

$$U_i = U_{i-1} + a_i(\Delta t_i), \Delta t_i = t_i - t_{i-1}, \tag{6}$$

$$X_i = X_{i-1} + U_{i-1}(\Delta t_i) + \frac{1}{2}a_i(\Delta t_i)^2, \tag{7}$$

where U_{i-1} is piston velocity at t_{i-1}, U_i is piston velocity at t_i, X_{i-1} is piston displacement at t_{i-1}, and X_i is piston displacement at t_i. When the moving piston finally hits a drill bit at the end of impact stroke, the piston's impact energy W can be calculated as:

$$W = \frac{1}{2}mU_f^2, \tag{8}$$

where U_f is the final velocity of the piston at its hit on the drill bit. The piston rebound velocity after its hit is the initial piston velocity at the start of next-round piston movement.

This study focuses on the dynamics of piston movement rather than the piston itself. Therefore, the piston is regarded as a rigid, intact object in our modeling scheme and no meshes or grids are generated to discretize the piston. Six Degrees of Freedom Solver from ANSYS Fluent is employed by importing User-defined functions (UDF) to calculate piston acceleration, velocity, and displacement based on the results of the airflow modeling.

3.3. Dynamic mesh generation

Structure of the GQ-400 DTH hammer was realized using Autodesk Inventor software before being exported into Integrated Computer Engineering and Manufacturing (ICEM) software for gridding. In this study, structured hexahedral grids are generated. Fig. 4a displays a 3D view of the real meshes generated by ICEM for numerical simulations. Fig. 4b is a 2D schematic view of the GQ-400 DTH hammer model. It is noted that Fig. 4b does not represent true sizes of the meshes. True size of the leakage gap between the piston and inner tube is 0.2 mm and the gap is represented by 4 layers of meshes with thickness 0.05 mm. Initial number of meshes (or mesh density) in a numerical model significantly impacts the model's accuracy. Generally, a higher mesh density would improve the accuracy but leads to a longer computation time. An optimum choice of mesh number that balances computation accuracy and efficiency is truly desirable. Herein we evaluate seven numerical models that are assigned different number of initial meshes. Table 3 lists the numbers of initial meshes used in these simulations and the corresponding simulation results including piston impact energy (in a single hit) W, piston impact frequency F, and air consumption rate Q. In the simulation, timestep size was defined as 1e−4 s to avoid the negative volume caused by piston displacement in one timestep exceeding mesh height. Maximum iteration number was set to be 200 per timestep to ensure the convergence in each timestep. Table 3 support that variations of impact energy vs. mesh number, impact frequency vs. mesh number, and air consumption rate vs. mesh number become minor when the number is elevated to 0.8 million and beyond. For instance, discrepancies of impact energy, impact frequency, and air consumption between the numerical model of 0.8 million meshes and the one of 2.0 million meshes are 2.8%, 1.8%, and 1.4%, respectively. The numerical models of 0.8 million meshes or more achieve almost the same accuracy. Table 3 further lists the computing time taken by the seven numerical models and verifies that more meshes in a numerical model would definitely require longer computation. The workstation used for simulations has a CPU processor with a base frequency 3.8 GHz, 10-

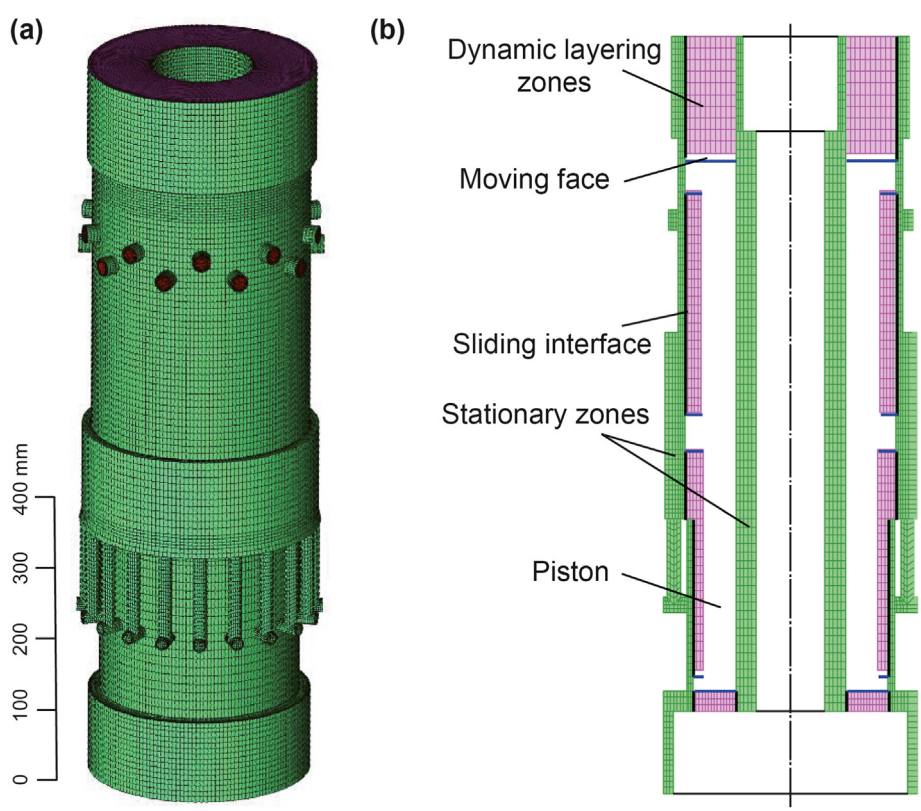

Fig. 4. (**a**) 3D view of initial meshes generated and (**b**) a 2D schematic view of meshes for the GQ-400 DTH hammer model.

Table 3
Effect of mesh numbers on the performance of numerical models.

Number of mesh elements, million	Impact energy W, J	Impact frequency F, Hz	Air consumption Q, m^3/min	Computation time, h	Time-step size, s
0.2	3784	11.70	46.56	2.34	1e−4
0.5	3687	11.45	46.17	7.73	1e−4
0.8	3964	11.70	47.89	13.27	1e−4
1.1	3879	11.56	48.24	22.56	1e−4
1.4	3918	11.63	48.93	27.08	1e−4
1.7	3855	11.49	48.37	31.42	1e−4
2.0	3855	11.49	48.56	35.60	1e−4

core, 20-thread, and 32 G RAM in total. It is noted that extra 1046.19 h are needed to finish all the simulations in this study if the mesh number is increased from 0.8 million to 2.0 million. In conclusion, when mesh number is and above 0.8 million, increasing the number of meshes has negligible influence on simulation results, but time consumption increases significantly. After weighing modeling accuracy and computing efficiency, we finally choose the initial number of meshes in this study to be 0.8 million.

$$P_i = P_{i-1} + \frac{R_g}{V_i}[T_i\dot{m}_i + T_{i-1}\dot{m}_{i-1}]\Delta t_i - \frac{P_{i-1}}{V_i}\Delta V_i, \Delta V_i = V_i - V_{i-1}, \tag{9}$$

$$T_i = T_{i-1}\left(\frac{V_{i-1}}{V_i}\right)^{k-1}, \tag{10}$$

$$\dot{m}_i = \begin{cases} R_f A_i \sqrt{\frac{k}{R_g}\left(\frac{2}{k+1}\right)^{\frac{k+1}{k-1}}}\ \frac{P_{in}}{\sqrt{T_{in}}}, & \frac{P_{out}}{P_{in}} \le \left(\frac{2}{k+1}\right)^{\frac{k}{k-1}} \\ R_f A_i P_{in}\sqrt{\frac{2}{R_g}\left(\frac{k}{k-1}\right)}\sqrt{\frac{1}{T_{in}}\left[\left(\frac{P_{out}}{P_{in}}\right)^{\frac{2}{k}} - \left(\frac{P_{out}}{P_{in}}\right)^{\frac{1+k}{k}}\right]}, & \frac{P_{out}}{P_{in}} > \left(\frac{2}{k+1}\right)^{\frac{k}{k-1}} \end{cases}, \tag{11}$$

Piston movement causes the gas chambers to expand or shrink. Numerical models need to account for the chamber space variations by updating meshes. Herein, a dynamic mesh approach is adopted to update the meshes as the piston moves. Dynamic mesh is an advanced method applied in the accurate modeling of fluid domains with geometries varying with time (Delannoy et al., 2007; Gao et al., 2018, 2019; Li et al., 2015; Pang et al., 2019; Zhang et al., 2019). Fig. 4b provides a 2D schematic view of dynamic meshes generated for the GQ-400 DTH hammer model. As can be seen in Fig. 4b, a computational domain around the piston can be divided into dynamic layering zones and stationary zones. Number and height of the meshes in a dynamic zone would vary when the piston moves, while all the meshes in the stationary zones remain unchanged. A sliding interface is further set on the path that the piston moves along. The piston can move back and forth along the interface without realigning meshes during a simulation. Fig. 5 gives an example of the dynamic meshing in response to piston movement. It is noted that mesh merging occurs at advancing piston surfaces while mesh split happens at retreating piston surfaces. The layer of meshes representing a moving face would expand or collapse in response to the recession or advance of the piston. The layer could expand until reaching the user-defined maximum mesh height and splitting into two layers. Similarly, the layer could collapse until reaching the user-defined minimum mesh height and merging into its adjacent layer.

4. Model verification

Numerical modeling in this study is compared against the theoretical model of Yin (2020). Yin (2020) calculated the gas pressure P_i in a chamber at the end of i-th time step (t_{i-1}, t_i) as:

$$V_i = V_{i-1} + \left[U_{i-1}(\Delta t_i) + \frac{1}{2}a_i(\Delta t_i)^2\right] \times A_{pi}, \tag{12}$$

where P_{i-1} is gas pressure at t_{i-1}, T_i is gas temperature at t_i, T_{i-1} is gas temperature at t_{i-1}, $\dot{m}_i$ is gas flow rate at t_i, $\dot{m}_{i-1}$ is gas flow rate at t_{i-1}, V_i is chamber volume at t_i, V_{i-1} is chamber volume at t_{i-1}, k is adiabatic index, A_i is effective outlet area of the chamber at t_i, P_{in} is gas pressure at the inlet of the chamber, P_{out} is gas pressure at the outlet of the chamber, T_{in} is gas temperature at the inlet of the chamber, R_f is flow resistance coefficient at the outlet of the chamber, U_{i-1} is piston velocity at t_{i-1}, a_i is piston acceleration at t_i, and A_{pi} is the area of the piston exposed to the chamber at t_i. In Yin's work (Yin, 2020), piston impact energy was calculated by taking the P_i from Eq. (9) into Eqs. (5)–(8).

Fig. 6 compares the performance of the hammer in Table 2 calculated by our numerical model against Yin's model (Yin, 2020). Fig. 6 displays the variations of impact energy vs. air supply pressure, impact frequency vs. air supply pressure, maximum stroke vs. air supply pressure, air consumption vs. air supply pressure, and energy efficiency vs. air supply pressure by the two models. Generally a higher air supply pressure leads to elevated pressures in hammer chambers and accordingly, drives hammer piston towards a further TDC. This is consistent with our numerical model as well as Yin's model in Fig. 6a and b: impact energy, impact frequency, maximum stroke, and air consumption all exhibit upward tends against air supply pressure.

Overall our numerical results match reasonably well with the modeling results of Yin (2020). Fig. 6a demonstrates that the two

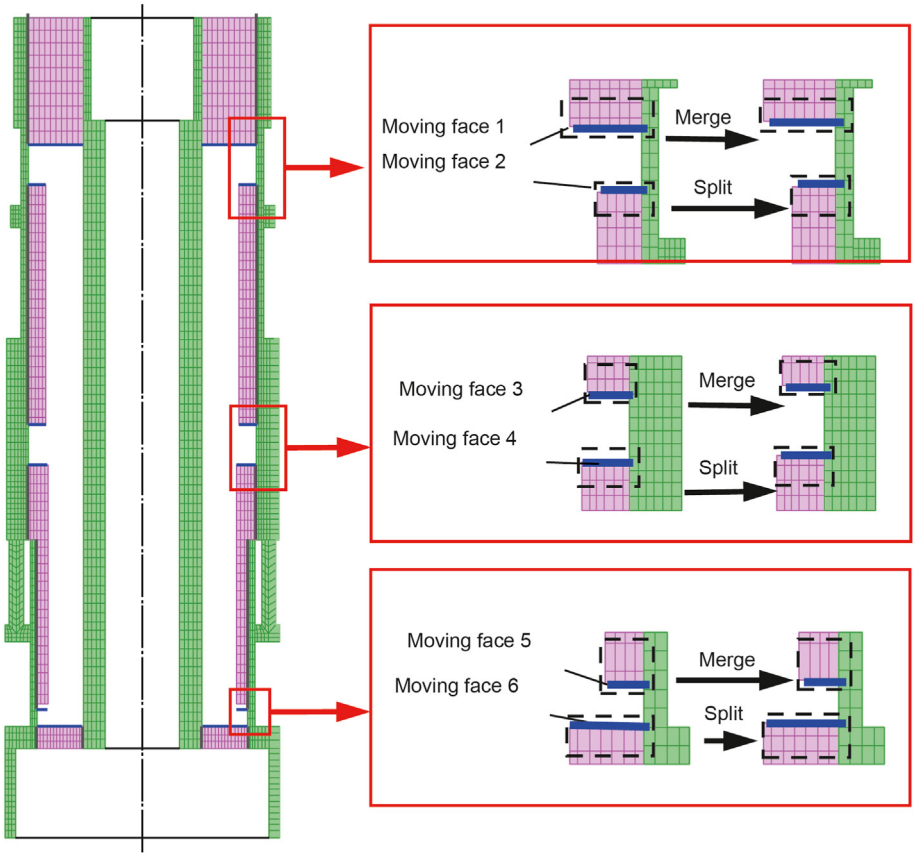

Fig. 5. An example of dynamic meshing when the piston moves up.

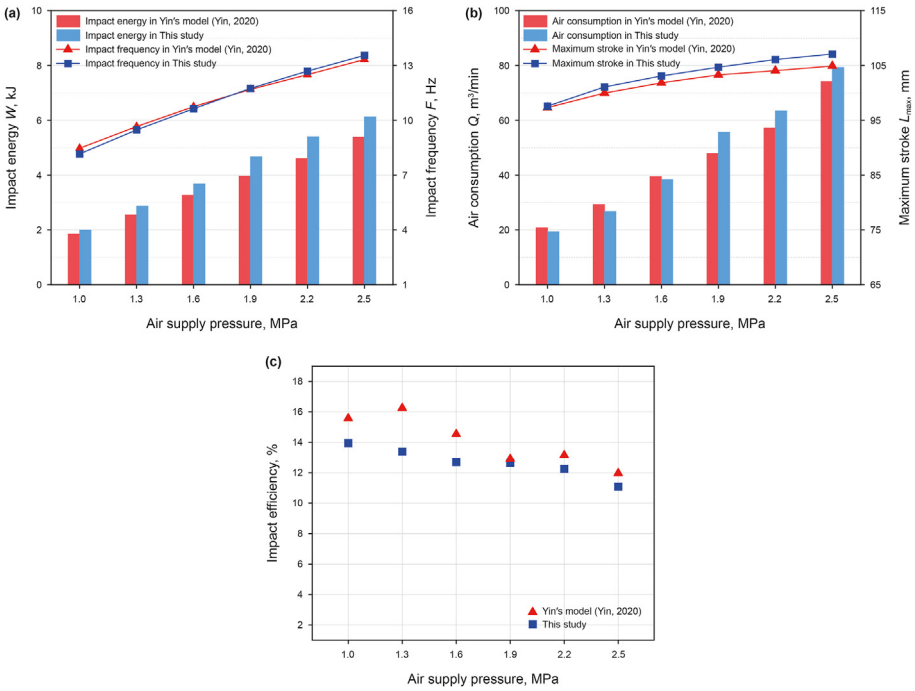

Fig. 6. Comparison between the numerical model in this study and the theoretical model by Yin (2020).

models provide truly close calculations of impact frequency and the maximum discrepancy of impact energy between the two models is 0.73 kJ at an air supply pressure of 2.5 MPa. Fig. 6b exhibits that discrepancy of maximum stroke between the two models increases slightly with the air supply pressure and the maximum discrepancy of air consumptions is 7.75 m^3/min occurring at an air supply pressure of 1.9 MPa. Fig. 6c demonstrates that impact efficiencies calculated in numerical simulations exhibit a downward trend as the air supply pressure increases while Yin's results (Yin, 2020) show a fluctuating trend. The maximum discrepancy of impact efficiency calculated by the two models is 2.86% at an air supply pressure of 1.3 MPa. We guess that the differences between the two models' results may partially arise from the different assumptions these models have made. For instance, Yin (2020) assumed that the pressure distribution in a chamber is always uniform, while our numerical model does not pre-assume uniform pressure distributions in chambers. Besides, impact efficiency is calculated with impact velocity, impact frequency, and air consumption. Therefore, the discrepancy of impact efficiency between Yin's model and this study in Fig. 6c is affected by the discrepancies occurring in Fig. 6a and b. This may further explain bigger discrepancies between Yin's model (Yin, 2020) and this study in Fig. 6c than in Fig. 6a and b.

5. Results and discussion

5.1. Dynamics of piston movement

Fig. 7a displays the typical variation of piston velocity vs. displacement from our numerical model of the hammer equipped with a 250-mm-sized piston groove (other structural parameters can be checked in Table 2) and Fig. 7b shows the pressure contours corresponding to each stage. Please note that positive and negative velocity refer to the upward and downward velocity, respectively. Overall, hammer piston experiences higher velocities in impact stroke than in return stroke. From Stage 1 to Stage 3, hammer front chamber has higher gas pressures than its rear chamber. As the piston moves up, air pressure in the rear chamber increases while the pressure of the front chamber decreases. The pressure difference between the two chambers narrows. In consequence, the increment of piston upward velocity experiences slowing down

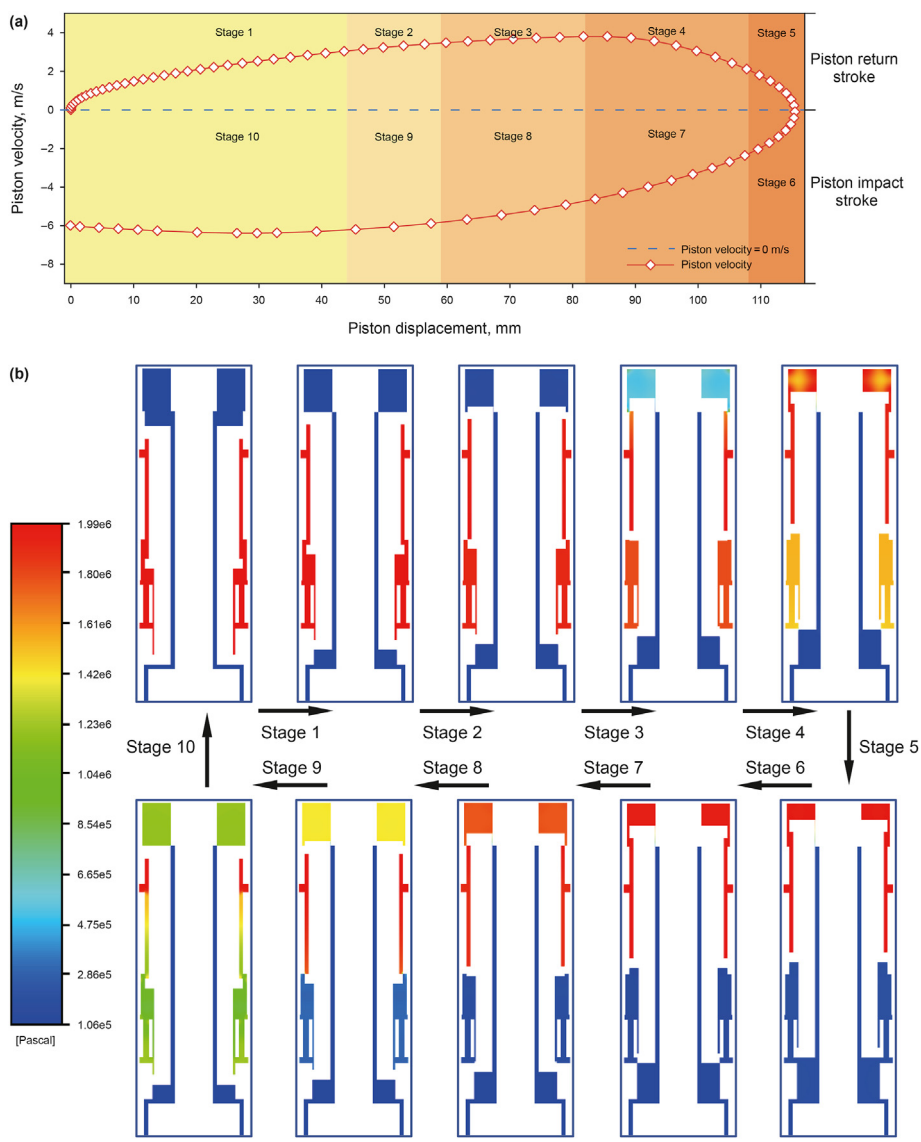

Fig. 7. (**a**) Piston velocity vs. displacement profile and (**b**) pressure contours in each stage calculated from a numerical simulation of piston return and impact stroke.

from Stage 1 to Stage 3. Piston upward velocity reaches its maximum at the displacement of 85.5 mm. Then from Stage 4 to about half of Stage 10, gas pressure of the rear chamber turns higher than the front chamber. Accordingly, the pressure difference between the two chambers creates negative accelerations. From Stage 4 to Stage 5, piston upward velocity gradually reduces to zero at TDC of 115.4 mm, the pressure in front chamber exhaust to its minimum. Piston velocity turns downward since Stage 6. The downward velocity keeps increasing and reaches its maximum at the displacement of 29.7 mm during Stage 10. Then the downward velocity starts to decrease but only for a very short period since the piston quickly hits a drill bit at the end of Stage 10.

5.2. Effect of hammer structure

In this section influences of a large-diameter pneumatic DTH hammer's structure on its impact performance as well as the dynamics of hammer piston movement are investigated in detail. Eight structural parameters including piston mass, rear chamber length, piston upper-end diameter, piston groove diameter, intake and exhaust stroke of the front chamber, and intake and exhaust stroke of the rear chamber are discussed herein. Air supply pressure is fixed to be 1.90 MPa, piston mass is set as 240 kg, and all the other parameters would take the default values listed in Table 2 unless otherwise specified.

5.2.1. Piston mass

Six pistons of 150 kg, 180 kg, 210 kg, 240 kg, 270 kg, and 300 kg, respectively, are taken into numerical simulations. Fig. 8 display variations of impact energy, impact frequency, maximum stroke, and air consumption against piston mass. As a piston becomes heavier, its impact energy and maximum stroke tend to drop slightly in Fig. 8a and b. However, an obvious reduction of impact frequency from 14.70 Hz to 10.41 Hz occurs when piston mass increases from 150 kg to 300 kg. Also, air consumption decreases from 59.39 m^3/min towards 44.67 m^3/min. We consider that the decrease in air consumption is resulted from the decline of impact frequency. Under a low impact frequency condition, the number of reciprocating piston motions is reduced, thereby decreasing air consumption.

Reduction of piston frequency in response to an increasing piston mass can be explained by the dynamics of piston velocity. Fig. 9 provides temporal profiles of piston velocity in one round of piston up-and-down movement. Fig. 9 demonstrates that the curve

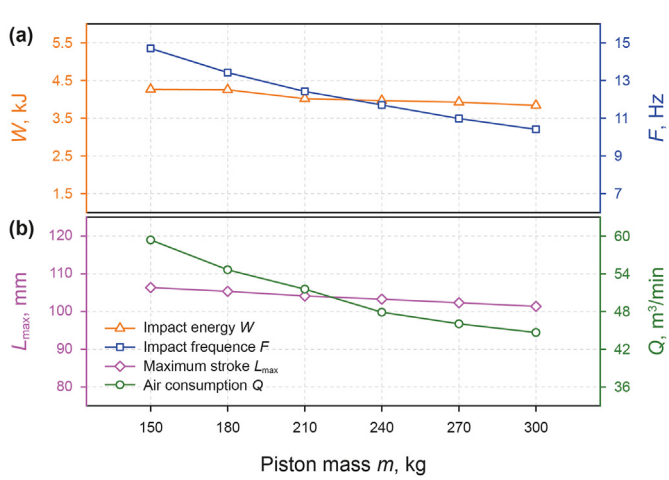

Fig. 8. Effect of piston mass m on (**a**) impact energy and impact frequency and (**b**) maximum stroke and air consumption.

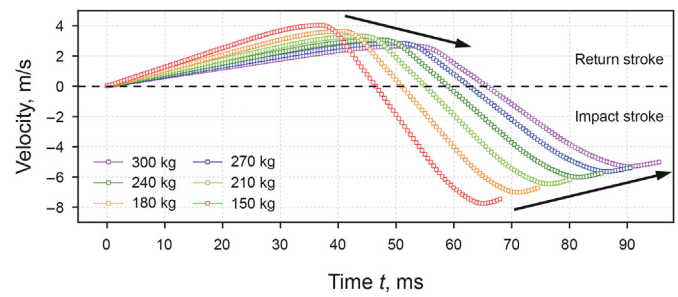

Fig. 9. Piston velocity vs. time profiles from the six numerical simulations of different piston mass.

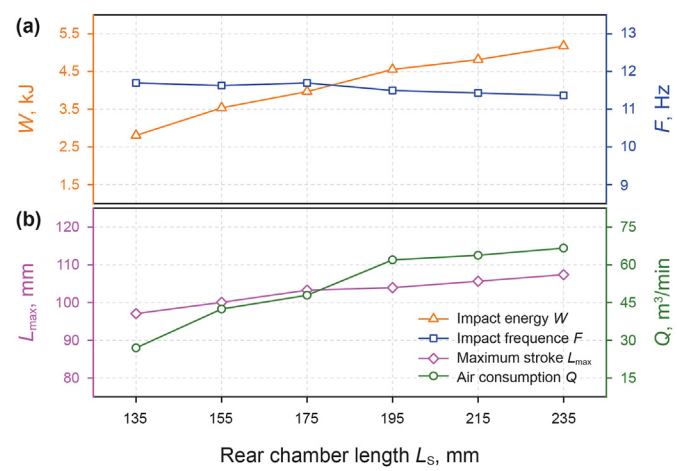

Fig. 10. Effect of rear chamber length L_s on (**a**) impact energy and impact frequency and (**b**) maximum stroke and air consumption.

of piston velocity vs. time is "compressed" and "extended" when a piston becomes heavier. As can be seen in Fig. 9, the time it takes for a piston to finish one round of movement increases from 68 ms to 95 ms when piston mass increases from 150 kg towards 300 kg.

5.2.2. Rear chamber length

Six values of rear chamber length L_s are examined in our numerical simulations. Fig. 10 shows data points of impact energy vs. rear chamber length, impact frequency vs. rear chamber length, maximum stroke vs. rear chamber length, and air consumption vs. rear chamber length, respectively, from the numerical simulations. Fig. 10a suggests that impact energy improves from 2.80 kJ to 5.17 kJ in response to an increasing chamber length from 135 mm to 235 mm. In contrast to impact energy, the variation of impact frequency vs. chamber length are quite marginal. As can be seen in Fig. 10b, the maximum stroke that a piston can travel increases slightly corresponding to a longer chamber length. The air consumption at a rear chamber length of 235 mm becomes 2.47 times higher than that at the chamber length of 135 mm. Usually a longer rear chamber would consume more air due to its bigger chamber volume. When the amount of the air in the rear chamber is fixed, a longer rear chamber leads to a lower air pressure inside and therefore, a smaller resistance to the piston upward movement. Hence, maximum stroke extends as the rear chamber length increases. Fig. 11 shows temporal profiles of piston velocity calculated with the numerical simulations. Fig. 11 supports that a longer rear chamber would expand a temporal velocity profile by enlarging both maximum upward/downward velocity and final impact velocity. The final impact velocity is improved from 4.83 m/s to

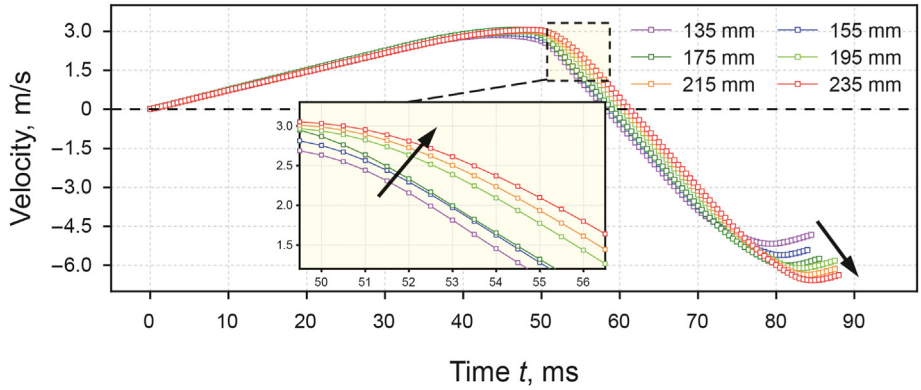

Fig. 11. Piston velocity vs. time profiles from the numerical simulations of different rear chamber length.

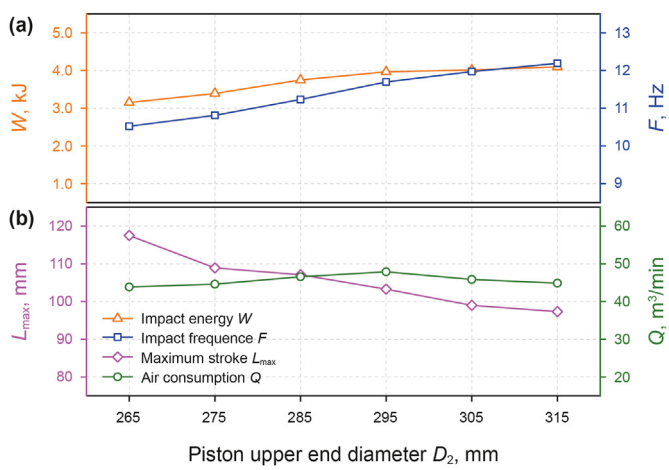

Fig. 12. Effect of piston upper-end diameter D_2 on (**a**) impact energy and impact frequency and (**b**) maximum stroke and air consumption.

6.38 m/s when rear chamber length increases from 135 mm to 235 mm, which is consistent with the increasing of impact energy in Fig. 10a. Fig. 11 also proves that a longer rear chamber could slightly prolong return stroke while negligibly influence the duration of impact stroke.

5.2.3. Piston upper-end diameter

Six numerical simulations under different piston upper-end diameters are completed. Fig. 12 displays data points of impact energy, impact frequency, maximum stroke, and air consumption against piston upper-end diameter from the numerical simulations. Fig. 12a shows that piston impact energy rises until the upper-end diameter reaches 295 mm from 265 mm. Then the impact energy remains almost stable although the upper-end diameter continues to increase. Piston impact frequency keeps increasing along with the piston's enlarging upper end. In Fig. 12b maximum stroke decreases with respect to a larger upper-end diameter. Air consumption tends to increase slightly when the upper-end diameter increases up to 295 mm but decreases lightly as the diameter continues to increase. This concave-downward characteristic of air consumption vs. upper-end diameter occurs from the superposition of ascending impact frequency in Fig. 12a and descending maximum stroke in Fig. 12b. Fig. 12a and b together suggests that piston impact energy and frequency can be improved by enlarging its upper end without consuming more air.

Fig. 13 provides the temporal profiles of piston velocity. It shows that a large upper end can prolong both return and impact stroke. When upper-end diameter is increased, piston upward velocity is reduced whereas the downward velocity is improved. Enlarging piston upper end increases the downward force from the air in the rear chamber. And the increment of this force slows down piston upward movement while accelerates the downward movement. Fig. 13 further displays that the increment of final impact velocity is marginal for the pistons with upper-end diameter increasing from 295 mm to 315 mm. This feature can explain the behavior of impact energy vs. upper-end diameter of (295 mm, 315 mm) in Fig. 12a.

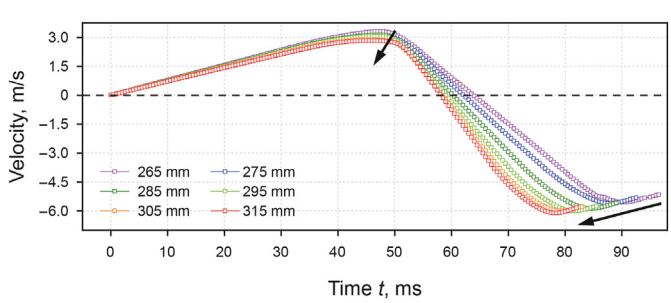

Fig. 13. Piston velocity vs. time profiles from the numerical simulations of different upper-end diameters.

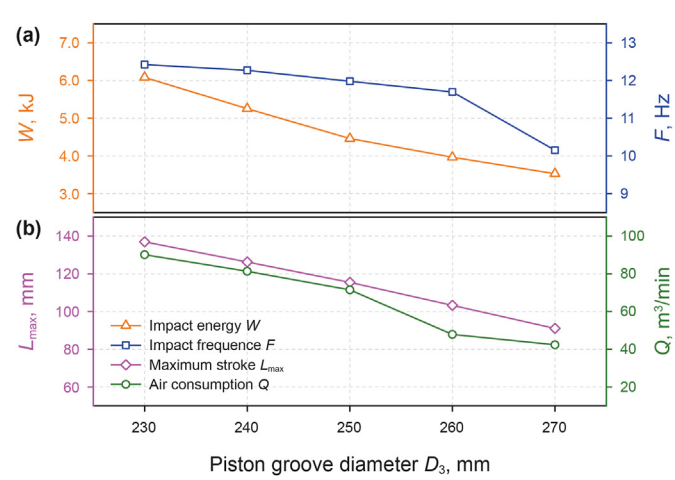

Fig. 14. Effect of piston groove diameter D_3 on (**a**) impact energy and impact frequency and (**b**) maximum stroke and air consumption.

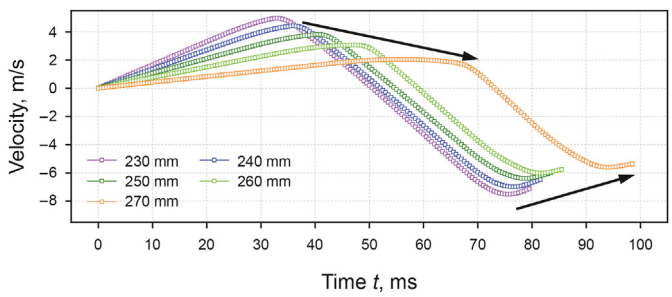

Fig. 15. Piston velocity vs. time profiles calculated from the numerical simulations of different groove diameters.

5.2.4. Piston groove diameter

Herein numerical simulations of six groove diameter values are completed. Fig. 14 displays data points of impact energy, impact frequency, maximum stroke, and air consumption against piston groove diameter from the numerical simulations. Fig. 14a suggests that piston impact energy keeps decreasing when piston groove becomes bigger. Piston impact frequency also experiences reduction when the groove diameter increases from 230 mm to 270 mm, especially from 260 mm to 270 mm. In Fig. 14b maximum stroke decreases linearly in response to an ascending groove diameter. Air consumption decreases from 90.13 m^3/min to 42.41 m^3/min along with an increasing groove diameter. And the biggest decrement of air consumption is observed from 250-mm diameter to 260-mm diameter.

Fig. 15 displays the temporal profiles of piston velocity from the six simulations. It suggests that a big groove would significantly extend the return stroke while negligibly affect the duration of impact stroke. Fig. 15 demonstrates that when a piston groove becomes bigger the curve of piston velocity vs. time is "compressed" and "extended" with the final impact velocity decreasing from 7.12 m/s to 5.36 m/s. This feature well justifies the characteristic of impact energy vs. groove diameter in Fig. 14a.

5.2.5. Intake stroke of the front chamber

Six numerical simulations of different intake stroke L_1 of the front chamber are completed. Fig. 16 displays the data of impact energy vs. intake stroke, impact frequency vs. intake stroke, maximum stroke vs. intake stroke, and air consumption vs. intake stroke, respectively, calculated by the numerical simulations. Fig. 16 suggests that variations of the intake stroke have marginal influence on the four indicators. When the intake stroke rises from 49 mm to 74 mm, impact energy varies in a very narrow range of (4.03 kJ, 3.86 kJ) and impact frequency is found to be in a range of (11.63 Hz, 11.49 Hz). Maximum stroke varies between 103.07 mm and 104.32 mm and air consumption is also observed to vary in a very narrow range of (46.99 m^3/min, 48.56 m^3/min). We conclude that the effect of the intake stroke of the front chamber on a hammer's performance is negligible.

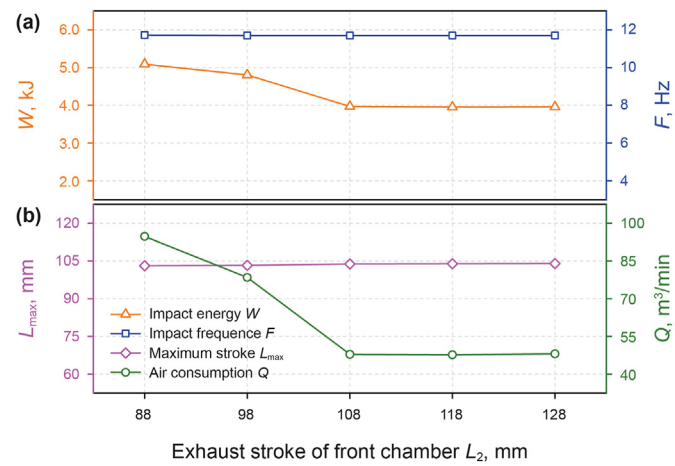

Fig. 17. Effect of the exhaust stroke of the front chamber on (**a**) impact energy and impact frequency and (**b**) maximum stroke and air consumption.

5.2.6. Exhaust stroke of the front chamber

Six values of the exhaust stroke of the front chamber L_2 are investigated with our numerical simulations. Fig. 17 shows the data points of impact energy vs. exhaust stroke, impact frequency vs. exhaust stroke, maximum stroke vs. exhaust stroke, and air consumption vs. exhaust stroke, respectively, calculated by numerical simulations. Fig. 17 demonstrates that the exhaust stroke has a negligible influence on piston impact frequency and maximum stroke. As the exhaust stroke increases, both piston impact energy and air consumption decrease first and then remain almost constant. This feature is resulted from the connectivity between front chamber and outlet channel. When the exhaust stroke is set in a range of (88 mm, 108 mm), air can be discharged freely once the

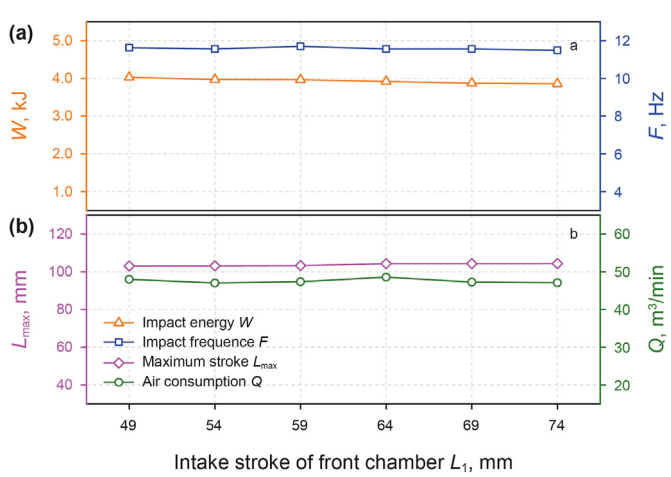

Fig. 16. Effect of intake stroke of the front chamber on (**a**) impact energy and impact frequency and (**b**) maximum stroke and air consumption.

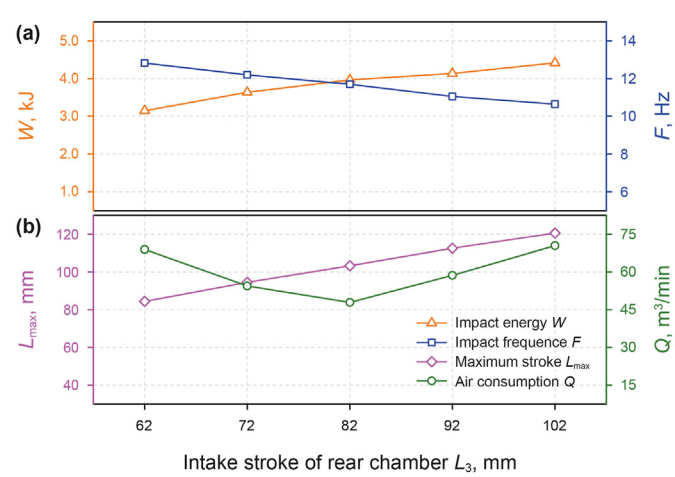

Fig. 18. Effect of the intake stroke of the rear chamber on (**a**) impact energy and impact frequency and (**b**) maximum stroke and air consumption.

front chamber is connected to outlet channel. As the exhaust stroke becomes longer, less air is pushed out of the front chamber once open to outlet channel. This hinders piston downward movement and reduces piston impact energy. When the exhaust stroke varies in a range of (108 mm, 128 mm), the front chamber is fully disconnected from outlet channel. Therefore, variation of the exhaust stroke can no longer affect piston movement.

5.2.7. Intake stroke of the rear chamber

Herein we complete six numerical simulations of different intake stroke of the rear chamber. Fig. 18 shows data points of impact energy vs. intake stroke, impact frequency vs. intake stroke, maximum stroke vs. intake stroke, and air consumption vs. intake stroke, respectively, calculated by the numerical simulations. It suggests that both piston impact energy and maximum stroke increase when the intake stroke elongates. Impact frequency decreases in response to a longer intake stroke from 12.82 Hz to 10.64 Hz. Furthermore, Fig. 18b shows a concave-upward variation of air consumption vs. intake stroke. This concave-upward trend is resulted from the superposition of descending impact frequency and ascending maximum stroke.

Fig. 19 provides the temporal profiles of piston velocity under six values of intake stroke. It displays that elongating the intake stroke would extend the duration during which a piston can stay at its maximum upward velocity. A piston can maintain its maximum upward velocity from 41.5 ms to 54.5 ms when the intake stroke is extended to be 102 mm. Correspondingly, the piston is allowed to move up through a longer distance, i.e., a larger maximum stroke, when the intake stroke becomes longer.

5.2.8. Exhaust stroke of the rear chamber

Six values of the exhaust stroke of the rear chamber L_4 are covered with our numerical simulations. Fig. 20 shows the data of impact energy vs. exhaust stroke, impact frequency vs. exhaust stroke, maximum stroke vs. exhaust stroke, and air consumption vs. exhaust stroke, respectively, calculated by the numerical simulations. It demonstrates that piston impact energy is reduced slightly from 4.30 kJ to 3.59 kJ when the exhaust stroke increases from 29 mm to 54 mm. Impact frequency remains almost stable around 11.60 Hz but maximum stroke increases from 99.26 mm to 105.76 mm. More air is consumed in response to an increasing exhaust stroke due to the ascending maximum stroke.

Fig. 21 provides six temporal profiles of piston velocity from the numerical simulations. Fig. 21 suggests that lengthening the exhaust stroke of the rear chamber would "lift up" a temporal velocity profile by increasing the maximum upward velocity and reducing the final impact velocity. Usually a longer exhaust stroke in the rear chamber would allow the duration of air discharge to last longer and reduce the chamber pressure. Low rear chamber pressure can create less resistance to piston upward movement,

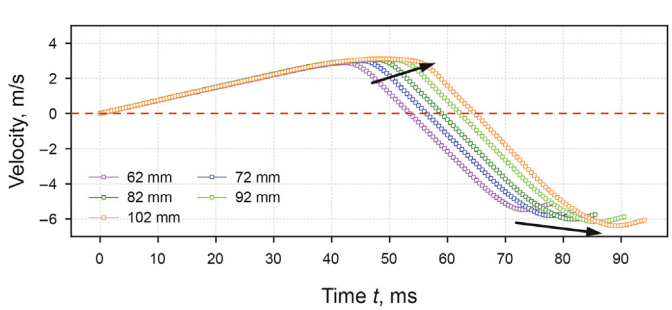

Fig. 19. Piston velocity vs. time profiles from the numerical simulations of different intake stroke of the rear chamber.

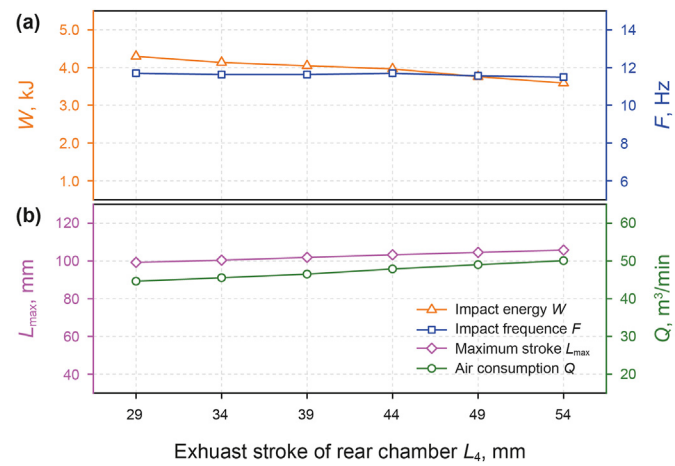

Fig. 20. Effect of the exhaust stroke of the rear chamber on (**a**) impact energy and impact frequency and (**b**) maximum stroke and air consumption.

making the piston upward velocity larger as well as generate less driven force to the piston downward movement, leading to lower final impact velocity.

Table 4 summarizes the behavior of DTH hammer performance in response to the variation of structural parameters. Table 4 indicates that changing the intake stroke of front chamber has negligible influence on hammer performance. And increasing the piston groove would lower all the four indicators. All the other six structural parameters demonstrate mixed effects on hammer performance. It is not an easy work to improve DTH hammer's performance considering the complexity of its response to the variations of these structural parameters.

6. Field test

In practical design of pneumatic hammers, a higher impact energy is not always included into design goals. Moderate impact energy output would extend the lifespan of a pneumatic hammer. In this study, a 400-mm-diameter DTH hammer with moderate impact energy around 2.50 kJ was designed for minimum air consumption rate with the help of numerical simulations. Impact frequency was fixed above 20 Hz in the hammer design. Table 5 lists chosen values of the eight structural parameters for the designed hammer. Simulated impact energy, impact frequency, and air consumption rate were 2.52 kJ, 21 Hz, and 47 m^3/min, respectively. The hammer was manufactured by Shanghai Jintai Engineering Machinery Co. and then applied in our drilling test.

The drilling test was carried out at SY-1 water well to check the DTH hammer's performance. SY-1 well was located in an unstable shallow formation of weathered sandstone, Qinshui County, Shanxi, China. Through the formation a borehole of 10-m depth was drilled using the designed GQ-400 DTH hammer. Fig. 22 gives a snapshot of the drilling site and the designed hammer. A TSJ-2600 rotary drill rig (see Fig. 22a) and two LUY-400-30 air compressors with total working capacity up to 80 m^3/min and 3 MPa were utilized in cooperation with the DTH hammer. Operation of the hammer was recorded on-site and hammer impact frequency was monitored in real-time using software Audacity. Hammer impact frequency was found to remain around 19 Hz when working stably. Average penetration rate in this drilling test was about 1.7 m/h, which was 1.7 times larger than that of conventional mud drilling in the same region. We conclude that the designed GQ400 DTH hammer is in good working condition and exhibits performance as expected by the numerical simulations.

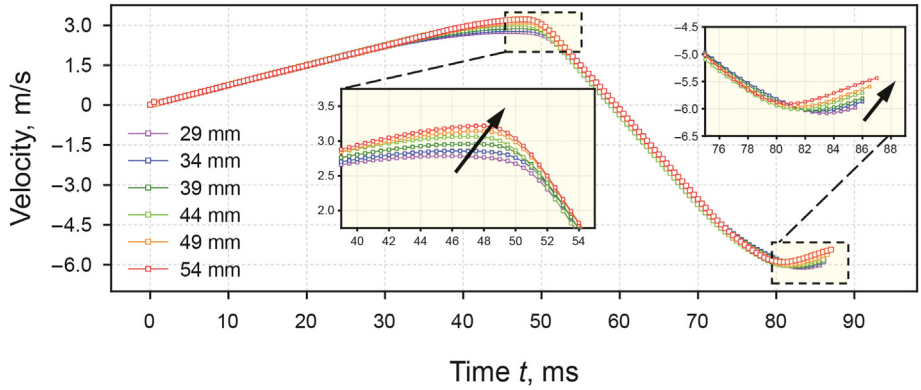

Fig. 21. Piston velocity vs. time profiles from the numerical simulations of different exhaust stroke values in the rear chamber.

Table 4
A summary on DTH hammer's response to its structure variation.

Ascending structural parameter	Impact energy W	Impact frequency F	Piston maximum stroke L_{max}	Air consumption Q
Piston mass	Marginal	Decline	Marginal	Decline
Rear chamber length	Rise	Marginal	Rise	Rise
Piston upper end diameter	Rise then stable	Rise	Decline	Rise then decline
Piston groove diameter	Decline	Decline	Decline	Decline
Intake stroke of front chamber	Marginal	Marginal	Marginal	Marginal
Exhaust stroke of front chamber	Decline then stable	Marginal	Marginal	Decline then stable
Intake stroke of rear chamber	Rise	Decline	Rise	Decline then rise
Exhaust stroke of rear chamber	Decline	Marginal	Marginal	Rise

Table 5
Characteristic sizes of the designed GQ-400 DTH hammer.

Piston mass M, kg	200
Rear chamber length L_s, mm	145
Piston upper end diameter D_2, mm	315
Piston groove diameter D_3, mm	260
Intake stroke of front chamber L_1, mm	39
Exhaust stroke of front chamber L_2, mm	92
Intake stroke of rear chamber L_3, mm	49
Exhaust stroke of rear chamber L_4, mm	34

7. Summary and conclusions

Dynamics of air flow as well as piston movement in the pneumatic DTH hammers that are larger than conventional ones are modeled numerically with ANSYS Fluent. RNG turbulent model and dynamic mesh method can fully describe the turbulent air flow and the associated piston movement in a DTH hammer. Numerical modeling is validated against empirical equations published in literature. Effects of eight structural parameters on hammer performance, including piston mass, rear chamber, piston upper-end diameter, piston groove, and lengths of intake and exhaust stroke in both front and rear chambers, are analyzed in detail with sets of numerical simulations. Based on the numerical simulations, a large GQ-400 DTH hammer has been designed for minimum air consumption rate and tested in a field drilling practice.

- Reducing piston mass can increase piston impact frequency and air consumption without influencing impact energy and maximum stroke, while elongating rear chamber would have negligible influence on impact frequency.
- Enlarging piston upper end can lead to a first increasing and then decreasing air consumption rate, while enlarging piston groove would keep reducing air consumption rate.

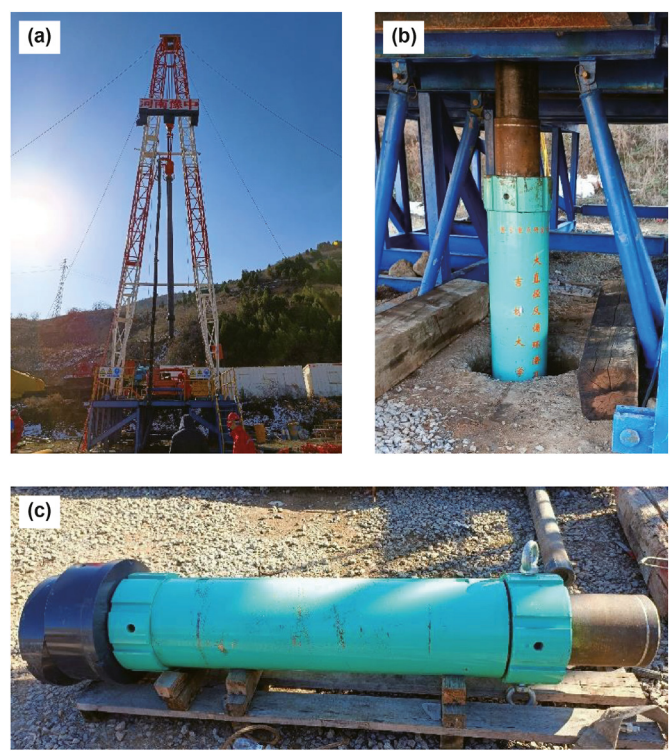

Fig. 22. The designed GQ-400 DTH hammer was applied in a drilling practice.

- For front chamber, changing the length of its intake stroke has marginal influence on hammer performance but extending its exhaust stroke makes both impact energy and air consumption rate decline first and then remain stable.

- For rear chamber, increasing the length of its intake stroke would decrease piston impact frequency but elongating its exhaust stroke has negligible impact on impact frequency.
- The GQ400 DTH hammer designed for reduced air consumption rate is in good working condition and exhibited performance as expected by the numerical simulations.

Author contribution

First author: Conceptualization, Methodology, Writing – original draft, Supervision, Project administration, Funding acquisition; Second author: Methodology, Validation, Formal analysis, Visualization; Third author: Methodology, Validation, Formal analysis, Visualization; Fourth author: Conceptualization, Methodology, Validation; Fifth author: Conceptualization, Methodology, Validation; Corresponding author: Methodology, Formal analysis, Writing – review & editing, Supervision.

Declaration of competing interest

The authors declare that they have no known competing fiscal interests or personal relationships that could have appeared to influence the work reported in this paper.

Acknowledgement

This work was supported by the Natural Science Foundation of Jilin Province (YDZJ202101ZYTS143) and National Key Research and Development Project of China (project No.2018YFC1505303).

References

ANSYS Inc, 2019. ANSYS Fluent Theory Guide, 2019R2.
Bu, C., Qu, Y., Cheng, Z., et al., 2009. Numerical simulation of impact on pneumatic DTH hammer percussive drilling. J. Earth Sci. 20 (5), 868–878. https://doi.org/10.1007/s12583-009-0073-5.
Cao, P., Chen, Y., Liu, M., et al., 2016. Analytical and experimental study of a reverse circulation drill bit with an annular slit. Adv. Mech. Eng. 8 (9), 1687814016669471. https://doi.org/10.1177/1687814016669471.
Cao, P., Chen, Y., Liu, M., et al., 2018. Optimal design of novel drill bit to control dust in down-the-hole hammer reverse circulation drilling. Arabian J. Sci. Eng. 43 (3), 1313–1324. https://doi.org/10.1007/s13369-017-2884-5.
Chiang, L.E., Elıas, D.A., 2000. Modeling impact in down-the-hole rock drilling. International. J. Rock Mech. Mining Sci. 37 (4), 599–613. https://doi.org/10.1016/S1365-1609(99)00124-0.
Chiang, L.E., Elıas, D.A., 2008. A 3D FEM methodology for simulating the impact in rock-drilling hammers. Int. J. Rock Mech. Min. Sci. 45 (5), 701–711. https://doi.org/10.1016/j.ijrmms.2007.08.001.
Chiang, L.E., Stamm, E.B., 1998. Design optimization of valveless DTH pneumatic hammers by a weighted pseudo-gradient search method. ASME. J. Mech. Des. 120 (4), 687–694. https://doi.org/10.1115/1.2829332.
Delannoy, Y., Barvinschi, F., Duffar, T., 2007. 3D dynamic mesh numerical model for multi-crystalline silicon furnaces. J. Cryst. Growth 303 (1), 170–174. https://doi.org/10.1016/j.jcrysgro.2006.12.075.
Franca, L.F., 2011. A bit–rock interaction model for rotary–percussive drilling. International. J. Rock Mech. Mining Sci. 48 (5), 827–835. https://doi.org/10.1016/j.ijrmms.2011.05.007.
Gao, Z., Wang, Y., Su, Y., et al., 2018. Numerical study of damaged ship's compartment sinking with air compression effect. Ocean Eng. 147, 68–76. https://doi.org/10.1016/j.oceaneng.2017.10.035.
Gao, Z., Wang, Y., Su, Y., et al., 2019. Validation of a combined dynamic mesh strategy for the simulation of body's large amplitude motion in wave. Ocean Eng. 187, 106169. https://doi.org/10.1016/j.oceaneng.2019.106169.
He, J.F., Sun, B.X., Liang, Y.P., et al., 2018. Research on suction capacity and dust suppression performance of a reverse circulation air hammer in tunnel drilling. Tunn. Undergr. Space Technol. 71, 391–402. https://doi.org/10.1016/j.tust.2017.09.008.
Juvani, K., Jokela, J., Lassheikki, T., et al., 2016. DTH steel casing drilling for pipeline construction in hard ground and rock conditions: technology and case examples. 11th Pipeline Technology Conference 2016. EITEP Institute, Hanover.
Kim, D.J., Oh, J.Y., Cho, J.W., et al., 2019. Design study of impact performance of a DTH hammer using PQRSM and numerical simulation. J. Mech. Sci. Technol. 33 (11), 5589–5602. https://doi.org/10.1007/s12206-019-1052-0.
Li, W., Lu, S., Liu, Y., et al., 2015. CFD simulation of the unsteady flow of a single coal log in a pipe. Can. J. Chem. Eng. 93 (11), 2084–2093. https://doi.org/10.1002/cjce.22312.
Lian, Z., Zhang, Q., Lin, T., et al., 2015. Experimental and numerical study of drill string dynamics in gas drilling of horizontal wells. J. Nat. Gas Sci. Eng. 27, 1412–1420. https://doi.org/10.1016/j.jngse.2015.10.005.
Lundberg, B., 1982. Microcomputer simulation of stress wave energy transfer to rock in percussive drilling. In International Journal of Rock. Mech. Mining Sci. Geomech. Abstract. 19 (5), 229–239. https://doi.org/10.1016/0148-9062(82)90221-2. Pergamon.
Luo, Y., Peng, J., Li, L., et al., 2016. Development of a specially designed drill bit for down-the-hole air hammer to reduce dust production in the drilling process. J. Clean. Prod. 112, 1040–1048. https://doi.org/10.1016/j.jclepro.2015.08.014.
Pang, B., Wang, S., Lu, C., et al., 2019. Investigation of cuttings transport in directional and horizontal drilling wellbores injected with pulsed drilling fluid using CFD approach. Tunn. Undergr. Space Technol. 90, 183–193. https://doi.org/10.1016/j.tust.2019.05.001.
Song, H., Shi, H., Ji, Z., et al., 2019. The percussive process and energy transfer efficiency of percussive drilling with consideration of rock damage. Int. J. Rock Mech. Min. Sci. 119, 1–12. https://doi.org/10.1016/j.ijrmms.2019.04.012.
Song, H., Shi, H., Li, G., et al., 2021. Numerical simulation of the energy transfer efficiency and rock damage in axial-torsional coupled percussive drilling. J. Petrol. Sci. Eng. 196, 107675. https://doi.org/10.1016/j.petrol.2020.107675.
Timonin, V.V., Alekseev, S.E., Karpov, V.N., et al., 2018. Influence of DTH hammer impact energy on drilling-with-casing system performance. J. Min. Sci. 54 (1), 53–60. https://doi.org/10.1134/S1062739118013341.
Versteeg, H.K., Malalasekera, W., 2007. An introduction to computational fluid dynamics: the finite volume method. Pearson Education, England.
Yakhot, V.S.A.S.T.B.C.G, Orszag, S.A., Thangam, S., et al., 1992. Development of turbulence models for shear flows by a double expansion technique. Phys. Fluid. Fluid Dynam. 4 (7), 1510–1520. https://doi.org/10.1063/1.858424.
Yao, S., Wang, X., Yuan, Q., et al., 2018. Transient-rate analysis of stress-sensitive hydraulic fractures: considering the geomechanical effect in anisotropic shale. SPE Reservoir Eval. Eng. 21 (4), 863–888. https://doi.org/10.2118/182006-PA.
Yin, Q., Peng, J., Bo, K., et al., 2013. Study on dust control performance of a hammer drill bit. Int. J. Min. Reclamat. Environ. 27 (6), 393–406. https://doi.org/10.1080/17480930.2013.787703.
Yin, Y., 2020. Pneumatic down-the-hole hammer. High Speed Pneumatic Theory Technol. II, 195–268.. Springer, Singapore.
Zhang, Q., Lian, Z., Lin, T., et al., 2016. Casing wear analysis helps verify the feasibility of gas drilling in direction wells. J. Nat. Gas Sci. Eng. 35, 291–298. https://doi.org/10.1016/j.jngse.2016.08.066.
Zhang, X., Luo, Y., Fan, L., et al., 2019. Investigation of RC-DTH air hammer performance using CFD approach with dynamic mesh method. J. Adv. Res. 18, 127–135. https://doi.org/10.1016/j.jare.2019.02.001.